

Probe the Localized Electrochemical Environment Effects and Electrode Reaction Dynamics for Metal Batteries using *in-situ* 3D Microscopy

Guangxia Feng^{1†}, Jiaming Guo^{1†}, Huajun Tian^{2†}, Zhao Li^{2,3}, Yaping Shi¹, Xiaoliang Li¹, Xu Yang¹, David Mayerich^{1*}, Yang Yang^{2,3,4,5*}, and Xiaonan Shan^{1*}

¹ Electrical and Computer Engineering Department, W306, Engineering Building 2, University of Houston, Houston, TX 77204, USA

² NanoScience Technology Center, University of Central Florida, Orlando, Florida 32826, USA

³ Department of Materials Science and Engineering, University of Central Florida, Orlando, Florida 32826, USA

⁴ Renewable Energy and Chemical Transformation Cluster, University of Central Florida, Orlando, Florida 32826, USA

⁵ Department of Chemistry, University of Central Florida, Orlando, Florida 32826, USA

† These authors contributed equally to this work.

Corresponding Authors

*E-mail: dmmayer2@central.uh.edu; Yang.Yang@ucf.edu; xshan@central.uh.edu;

Abstract

Uncontrollable dendrite growth is tightly related to non-uniform reaction environments. However, there is a lack of understanding and analysis methods to probe the localized electrochemical environment (LEE). Here we investigate the effects of the LEE, including localized ion concentrations, current density, and electric potential, on metal plating/stripping dynamics and dendrite minimization. A novel *in-situ* three-dimensional (3D) microscopy was developed to image the morphology dynamics and deposition rate of Zn plating/stripping processes on 3D Zn-Mn anodes. High quality 3D morphology maps were created using a multi-platform reconstruction framework. Using the *in-situ* 3D microscope, we directly imaged the electrode morphology changes during the reactions and obtained Zn deposition rate maps at different time points. We found that reaction kinetics are highly correlated to LEE and electrode morphology. To further quantify the LEE effects, the digital twin technique was employed that allows us to accurately calculate the electrochemical environments, such as localized ion concentrations, current density, and electric potential, which cannot be directly measured from the experiments. It is found that the curvature of the 3D electrode surface will determine the LEE and significantly influence reaction kinetics. This provides us a new strategy to minimize the dendrite formation by designing and optimizing the 3D geometry of the electrode to control the LEE.

This is the author manuscript accepted for publication and has undergone full peer review but has not been through the copyediting, typesetting, pagination and proofreading process, which may lead to differences between this version and the [Version of Record](#). Please cite this article as [doi: 10.1002/aenm.202103484](https://doi.org/10.1002/aenm.202103484).

This article is protected by copyright. All rights reserved.

1. Introduction

Rechargeable electrochemical batteries are extremely successful energy storage devices that have transformed the portable electronics industry,^[1, 2, 3, 4, 5] electric vehicles,^[6, 7] and smart grids.^[2, 8, 9] However, the uncontrollable dendrite growth initiated from electrolyte/electrode interfaces is the biggest challenge for rechargeable electrochemical systems, causing safety concerns and posing formidable barriers to the reliable power system for practical applications.^[10, 11, 12, 13, 14, 15, 16, 17, 18, 19, 20] Metal plating and stripping are complicated processes involving multiple electrons and mass transfer processes, including electron transfer across the electrode/electrolyte interface, mass transfer from solution onto the electrode surface, and surface diffusion.^[21, 22, 23, 24, 25, 26, 27] These processes are interconnected and determined by the local electrochemical environments (LEEs), including localized ion concentrations and current density, electric potential distributions, and surface diffusion coefficient. For example, the metal ions' diffusion and transportation, electrochemical potential and current density distributions on a 3D electrode are totally different with those on a flat electrode surface. In addition, LEEs are dynamically changing during the plating and stripping processes. The metal deposition will alternate the electrode geometry, consume the ions in the electrolyte, and vary the current density distributions in the entire reaction process. Therefore, it is important to monitor the entire process of metal deposition and stripping processes.

The current understanding of electrode reactions and dendrite formation is mostly based on the characterization of electrode morphology at the end of the reactions using morphology-based imaging methods such as scanning electron microscopy (SEM),^[28, 29] transmission electron microscopy (TEM),^[30, 31, 32, 33, 34, 35, 36, 37] and cryoelectron microscopy (cryo-EM).^[38, 39] Only a static morphology image of the electrode is obtained, missing important geometry changes and dynamics. Recent advances in instrumentation have led to some *in-situ* and *in-operando* studies of dendrite formation using nuclear magnetic resonance spectroscopy, transmission electron, and transmission X-ray microscopy.^[40, 41, 42, 43] However, these studies only provide the electrode cross-section changes during the reactions, while the 3D geometries are key to understanding LEEs. Atomic force microscopy (AFM) has been used to image the electrode reaction dynamics.^[37, 44] However, the slow scan speed and the tip-sample convolution affect its ability to probe large aspect ratio 3D electrode surfaces. Recently, synchrotron X-ray computed tomography (SXCT) has been used to study electrode tomography *in-operando*.^[45] Multi-scale visualization of dendrite growth, size, and branches have been achieved. However, the access to the synchrotron imaging beamline is limited which could affect its broad adaptations in research. In addition to the morphology characterization, we also need to measure and characterize the local electrochemical reaction conditions, such as local ion concentration and current density, potential distributions, and local deposition rate. However, most of these parameters cannot be directly measured.

In this paper, a novel optical based *in-situ* 3D microscope is developed to image the morphology changes in the plating and stripping processes throughout the entire reaction process. A $200 \times 200 \times 80 \mu\text{m}$ volumetric image of 3D morphology can be obtained within 3 seconds using the *in-situ* 3D microscope. High quality 3D morphology maps were created with a multi-platform reconstruction framework that will eliminate the optical spikes generated by non-uniform deposition and H_2 bubbles. Using this imaging system, we have mapped the 3D morphology changes of Zn-Mn alloy electrode during the Zn plating and stripping processes. We found that the Zn deposition is not uniform, and the deposition thickness is highly related to LEE. To further analyze the data, we created the Zn growth rate maps at different time points from the 3D geometries. The results showed that the deposition/stripping rates are location dependent and are highly correlated to the LEE effects and the electrode geometry. To obtain the localized ion concentrations, electric potential distributions, and current density (LEE parameters), we employed the digital twin technique to build a virtual replica of the real 3D Zn-Mn electrode. 3D morphology of the electrode was imported into a COMSOL Multiphysics model and the LEE parameters were calculated at different times. The results showed that the electrode morphology will determine the localized ion concentration distribution and

localized current density, and significantly influence the local Zn deposition/stripping rates. We found that the curvature of 3D electrode surface is the critical factor that will influence the reaction kinetics and dendrite formations. In the end, the Zn nucleation density and distributions were extracted and studied as well. The results obtained in this paper provide us a new strategy to minimize the dendrite formation by controlling the LEEs and optimizing the electrode geometry.

2. Results and Discussion

2.1. In-situ Optical 3D Imaging

An optical system was developed to image 3D morphological changes in the Zn-Mn alloy electrode during electrode reactions. The *in-situ* real-time 3D microscope is based on linearly scanning the objective-sample distance, imaging samples at different planes, and reconstructing the height maps for each pixel (**Figure 1**) in the reaction process. At a given imaging plane, only a thin layer of the 3D electrode will be in focus (Figure 1a). By sequentially changing the objective-electrode distance, different planes of the 3D structure will be imaged and saved (Figure 1a). A home-built motorized scanning stage (Figure S1, Supporting Information) is used to control the movement of the sample stage, and the camera frame rate and stage scanning speed is carefully selected to obtain enough cross-section images. In this work, the vertical interval between two images is optimized to be around 200 nm for best height detection accuracy (Figure S2, Supporting Information). In addition, the mechanical drift of the stage is minimized by decreasing the stage weight, and a drift correction algorithm is developed and used to correct the additional drift (Figure S3, Supporting Information). After scanning the sample in the entire vertical range, the 3D morphology will be extracted from the image stack using variance and wavelet transfer methods (Figure 1b).^[46, 47]

The morphology of Zn-Mn electrode was obtained using *in-situ* optical 3D microscopy and compared with SEM. The Zn-Mn electrode, which has three dimensional structures on the surface, has shown good capabilities to minimize Zn dendrite formation by controlling the reaction kinetics using its 3D morphologies.^[48] In this paper, we studied the LEEs created by the 3D structure and studied their capabilities to control the reaction kinetics and minimize of dendrite formation. The 3D electrode is fabricated using electrodeposition of Zn-Mn alloy performed in two-electrode electrochemical cells by a galvanostatic method. A $200 \times 200 \times 80 \mu\text{m}$ volume is scanned using the *in-situ* 3D microscope. The 3D morphology of the Zn-Mn alloy electrode is shown in Figure 1b. Due to hydrogen generation during the Zn-Mn alloy electrode fabrication process, protruding (white arrows in Figure 1b) and trench (black dashed circles in Figure 1b) regions have been created, and these 3D geometries will define the localized reaction environments and control reaction kinetics. To compare and verify our 3D microscope, the SEM image of the same location is obtained (Figure 1c). The protruding (white arrows in Figure 1c) and trench regions (black dashed circles in Figure 1c) can be identified in the SEM image and the shape of these morphologies perfectly matches those in the optical 3D image (Figure 1b). Although the spatial resolution of optical microscope is not as good as SEM, our 3D optical microscope provides a solution to perform *in-situ* 3D mapping during the Zn deposition processes, which allows us to image the morphology changes with sub micrometer spatial resolution in the entire reaction process. In addition, it is still difficult to perform SEM imaging in aqueous solutions and reconstruct a 3D morphology when the Zn deposition is happening. Figure 1d-g show the corresponding 3D morphology and the SEM image at zoomed-in areas of the 3D substrate. There are no obvious contrasts in the SEM images (Figure 1d-e), while the morphologies in the 3D optical image clearly show the height differences (Figure 1f-g).

To image the 3D morphology dynamics of a Zn-Mn electrode during the Zn deposition process, we have carefully designed the electrochemical cell to allow optical access to the region of interest without the disturbance of the reactions. In this design, objective, top, and bottom electrodes were all immersed in the electrolyte (Figure 1a left). Since the visible light cannot penetrate through the thick Zn alloy electrodes, we extended the bottom electrodes and imaged the 3D morphology changes on

this extended area. Note that the extended area is not directly facing the top electrode, which could decrease the current density in the area and varies the electric field distribution. To minimize this effect, the observation window was chosen as close as possible to the projection of the top electrode. Due to the limitation of the light beam diameters, the observation region is about 200-400 μm away from the edge of the top electrode. This is significantly smaller than the top and bottom electrode separation ($\sim 2\text{ mm}$), and the current density and electric field distribution in the observation area is similar to those inside the electrode area. To confirm our estimation, a COMSOL model was built to simulate the current density and electric field distribution in the extended area (Figure S4, Supporting Information). Comparing with the area inside the projection of the top electrode, the current density in the observation area only decreased by 5%. This result further verified that the observation area could represent the changes inside the battery electrodes. During the Zn plating and stripping processes, the 3D morphologies are continuously scanned and recorded. The reaction will change the electrode geometry constantly, even within a single scan. To minimize the morphology change in one scan, we increase our stage scanning rate and achieve an 80 μm vertical scan within 10 s. The geometry changes within 10 s are insignificant comparing with the total deposition time (1000~2000 s); generally, less than 180 nm in thickness even with 80 mA/cm^2 current density.

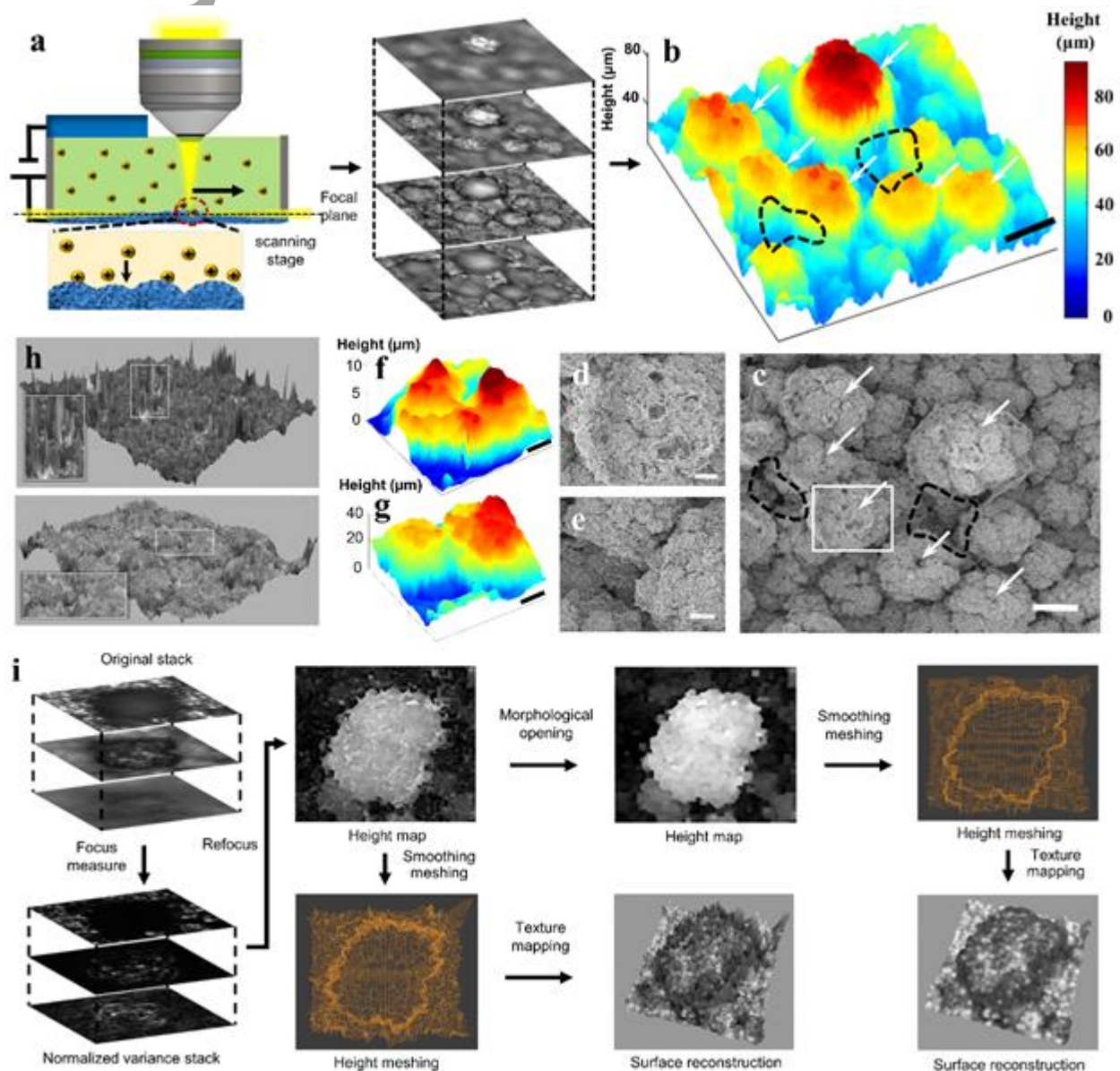


Figure. 1 In-situ 3D optical microscope. (a) Experimental setup and imaging stacks obtained from the microscope. (b) Reconstructed 3D morphology. (c) The corresponding SEM image. In (a-c): white arrows pointed to protruding regions, and black dashed line circled out the trench regions. (d-g) SEM and the corresponding 3D morphology of two zoomed in regions. The regions are marked with white rectangular in (c). (h) The reconstructed 3D morphology with spikes (top) and without the spikes (bottom). The bottom figure is reconstructed using our multi-platform framework. (i) The multi-platform framework for 3D reconstruction. Scale bars: 30 μm for (b) and (c), and 5 μm for (d-f).

2.2. Multi-platform 3D Reconstruction.

Plating and stripping generate free-floating hydrogen bubbles that interfere with digital refocusing. For instance, bubbles appear as saturated blobs in the image that are often erroneously classified as in-focus features using traditional methods.^[46, 47] Since hydrogen bubbles could flow through our imaging region, and this will lead to misclassification, outliers, or spikes in the refocused height map (Figure 1h top). In addition, newly deposited Zn substrates often have a much higher reflectivity to the impinging light, which also impairs focus evaluation and contributes optical spikes to the refocused map. Spikes that are located near the extrema would dramatically hinder three-dimensional visualization of the surface profile due to the elongated viewport.

To extract the actual surface profile, a multi-platform refocusing framework was developed and summarized as follows (Figure 1i). An image stack of 80 μm in depth was acquired using the proposed 3D microscope. The corresponding focus measures were computed based upon a modified variance metric,^[49, 50] in which each pixel receives a unique variance value provided by its surrounding pixels. Note that the variance kernel was adaptively defined by the shape and size of the target (ex. nucleus) to improve resolution. Since the variance matrix outlines high-frequency features, a sharper image produces a larger variance value. All in-focus positions were identified by finding the maximum values vertically and then reallocated to create a visually flat image. Next, a modified morphological opening algorithm was applied to remove outliers from the contaminated height map. Note that the structuring element used for convolution was also adaptively created based on the shape and size of the target to enhance performance. Once the refocused image and cleaned height map were obtained, a 3D model was generated using Blender via polygon meshing and texture mapping. The entire processing was implemented in Python and partially accelerated using graphic processing unit (GPU)-based methods.

2.3. Visualization of Zn Plating/stripping Dynamics on 3D Zn-Mn Electrode.

The 3D morphology will determine the LEEs and influence the reaction kinetics. Therefore, to fully understand the LEEs effects on the Zn deposition, we must image the morphology changes of the electrode during the reaction. To study the Zn plating process, an 80 mA cm^{-2} current was applied through the electrodes while the 3D optical microscope continuously scanned the surface to map morphology changes. Video 1 shows the 3D morphology of the Zn-Mn electrode during the entire Zn deposition process and demonstrates the capability of our 3D optical microscope to image the geometric changes in the reaction. The video shows the height of entire surfaces increases during the reaction, as well as non-uniform Zn deposition. **Figure 2a-c** show snap shots of the Zn-Mn electrode's morphologies video (Video 1 and Video 6, Supporting Information) at 0 s, 770 s, and 1460 s, respectively. First, there is no dendrite formed on the electrode surface (Figure 2c), even after 1460 s of Zn deposition under the large current density, which suggests that the Zn-Mn electrode has the capability to minimize dendrite growth. Second, the height of the entire electrode surface was elevated due to the deposition of the Zn. However, it is difficult to assess the geometry dependence of Zn deposition directly from the 3D morphology maps (Figure 2a-c). We have subtracted the initial electrode morphology from the 3D morphology video and only focus on the height changes caused by

the Zn deposition (Video 2, Supporting Information). Figure 2d-f show the snap shots of height change at 40 s, 770 s, and 1460 s, respectively. These figures show that some locations have significantly more deposition than other regions. This demonstrates that the deposition rate of Zn is not uniform and highly related to the location and the LEEs.

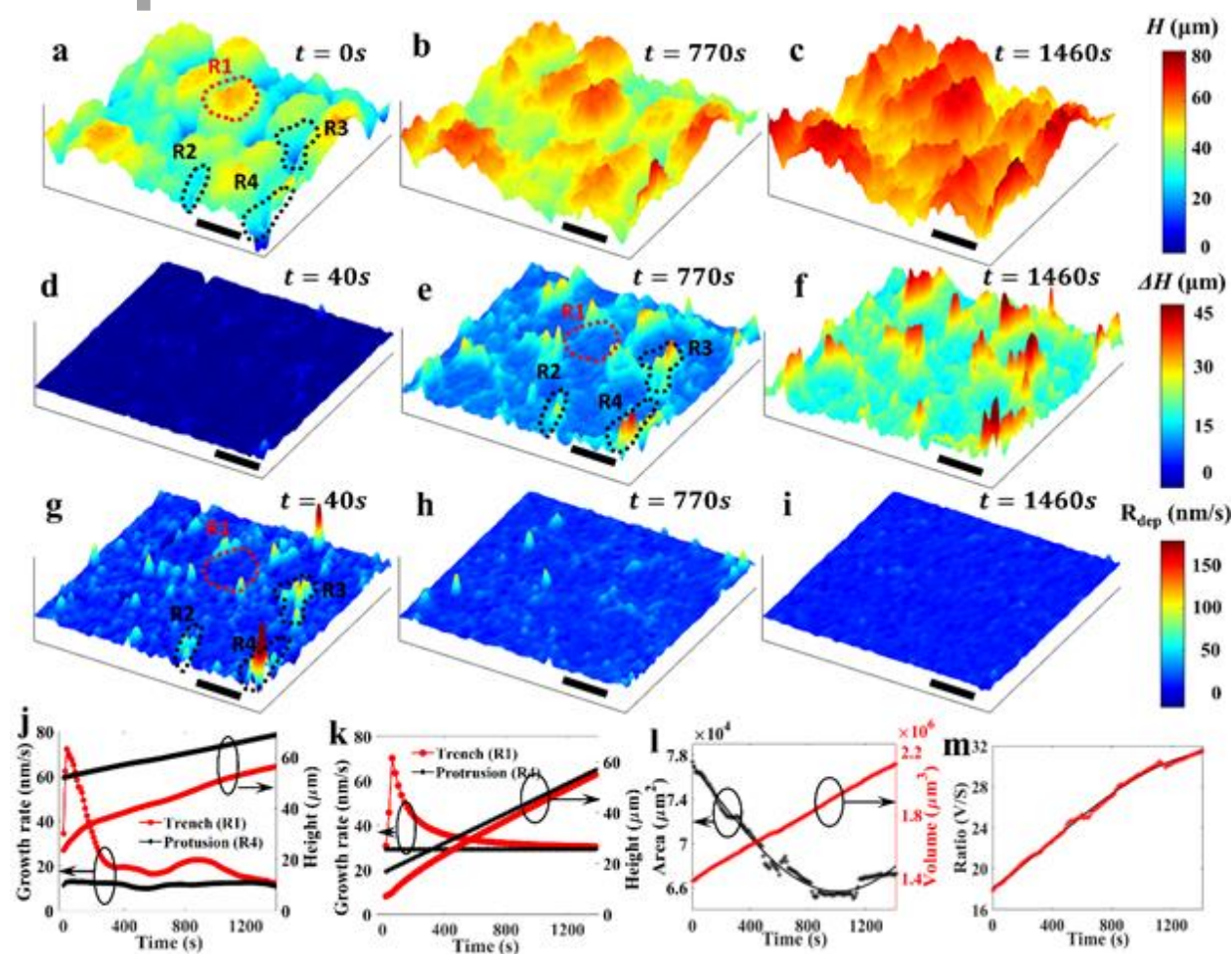


Figure. 2 Visualization of Zn plating/stripping dynamics. (a-c) The electrode morphology evolution after 0s, 770s, and 1460s of Zn plating with 80 mA cm^{-2} . The protruding region (R1) is circled with the red dashed line, and trench regions (R2-R4) are circled with a black dashed line in (a). (d-f) The deposited thickness maps after 40s, 770s, and 1460s of Zn plating. (g-i) The deposition rate map at 40s, 770s and 1460s. Scale bars in A-I: $30 \mu\text{m}$. (j) The growth rate and height change responses in the protruding region (R1) and trench region (R4). (k) The growth rate and height change responses in the protruding region and trench region were obtained from COMSOL simulation. (l) Electrode area and volume change over time. (m) Volume to surface ratio over time.

To further understand the geometry effect on deposition rate, different regions were selected for detailed analysis. 3D Zn-Mn alloy electrodes have two types of geometries: the protruding regions that are convex out of the substrate (R1 region in Figure 2a, circled with red dashed line) and the trench regions that are concave into the substrate (R2-R4 regions in Figure 2a, circled with black dashed line). The protruding regions have smaller curvatures (or geometry slopes) which could lead to a smaller local current density and a smaller Zn deposition rate. On the other hand, the trench regions have larger slopes and higher electrode surface areas per volume which could lead to a much larger current density and a faster Zn deposition rate. Comparing the height change map at different time points (ΔH , Figure 2d-f), we can clearly see that the Zn deposition at trench regions (R2-R4 in Figure 2e) is much faster than other regions. Protruding regions (R1 in Figure 2e) also grew during the Zn

deposition and had a mild height increase. In addition, even within the trench regions, the deposition rate is not constant. For example, the R2 region in Figure 2e has shown a much smaller thickness increase than the R3 and R4 regions.

The Zn growth rate maps (Video 3, Supporting Information) will further help us understand the LEEs effects and they can be easily calculated by subtracting two adjacent 3D morphologies of the electrode. Figure 2g-i show the Zn growth rate maps at 40 s, 770 s, and 1460 s. As we expected, the growth rate is not uniform across the electrode surface. In the early stages of the depositions, the trench regions have a much larger deposition rate (~70-150 nm/s in R2-R4 regions in Figure 2g) than the protruding regions (~40 nm/s in R1 region in Figure 2g). During the reaction, the protruding region reaction rate does not change significantly (~35-30 nm/s in R1 region in Figure 2h-i). However, the deposition rate in trench regions decays (~55-60 nm/s in R2-R4 in Figure 2h) and eventually returns to a level similar to the protruding regions (~35 nm/s in R2-R4 in Figure 2i). This observation can be explained as follows: at the beginning of the reaction, the trench region has more electrode surface area per volume, which leads to a higher deposition rate. The steeper trench will have faster deposition of the Zn (R2 vs. R4 in Figure 2g, we will discuss it more in the next section). As the reaction continues, the steeper trench will fill more quickly than other regions, and the slope of the trench will decrease. This results in a decrease in deposition rate in these trench regions. On the other hand, the morphology of the protruding regions does not change much throughout the reaction process, and neither does the deposition rate. These observations indicate that the Zn deposition is determined by the geometry and the localized electrochemical environments created and controlled by the geometry. Therefore, we can utilize the geometry and the associated LEEs to control the reaction kinetics and Zn deposition location to minimize dendrite formation.

The heights and Zn deposition rates of a protruding region (R1 in Figure 2a) and a trench region (R4 in Figure 2a) were plotted over time in Figure 2j. The Zn deposition rate in the protruding region is around 16 nm/s, which is constant throughout the entire deposition process. The deposition rate in the trench region is about 4 times higher (~60 nm/s) than the protruding region in the early stage of deposition. The deposition rate in the trench region quickly decays and eventually regress to the same level as the protruding region. We developed a finite element method model using COMSOL Multiphysics to understand the dynamics of the growth rate. The result (Figure 2k) matches well with our experimental results, suggesting that this is indeed caused by geometry changes in the reaction. We have also noticed that there is a sharp jump in growth rate on the first two points in both experiments (Figure 2j) and simulation results (Figure 2k). This effect is more pronounced in the trench region than in the protruding region. We have plotted the ion distributions from the COMSOL model (Figure S5 and Video 7, Supporting Information) and found that the Zn ions concentrations are significantly decreased in the trench region during the initial reaction. This ion depletion created a unique localized electrochemical environment that will increase the concentration gradient and the mass transport of the Zn ions.

The increase of the electrode surface-to-volume ratio could be an early sign of dendrite formation.^[45] Since we have the geometry information at all stages of the reaction, we have calculated the surface area, electrode volume, and surface-to-volume ratio (Figure 2l-m). The electrode surface area initially decreased and then stabilized toward the end of the reaction. This is because the Zn deposition will quickly fill up the deep trench regions and reduce the surface area. At the end of the deposition, the growth rate is constant everywhere (Figure 2i) and therefore, the surface area is stabilized. On the other hand, the volume is increasing during the entire reaction. As a result, the ratio of surface to volume increase with almost a constant speed which indicates that there is no obvious dendrite formed on the surface. This data also verify that the 3D Zn-Mn alloy electrode could control the reaction by LEEs and minimize the Zn dendrite formation.

The Zn stripping process was studied using *in-situ* 3D optical microscopy as well. Zn was deposited onto the Zn-Mn electrode for 1500 s before an 80 mAcm⁻² current was applied to strip the deposited Zn layer. The 3D morphology of the electrode surface was imaged throughout the reaction (Video 4, Supporting Information). **Figure 3** shows the 3D morphologies of the electrode (a) – (c) at 0, 770s and 1300 s, and the accumulated height change maps (d)-(f) at 210 s, 770s, and 1300 s,

respectively. The stripping process does decrease the average height of the electrode. However, the height change is not as significant as the deposition process, which is due to the side reactions. It is interesting to note that the stripping process is a reverse symmetric process to the Zn deposition. At the early stage of the stripping process, the thickness decreases, and the stripping rate is uniform (Figure 3d) across the entire electrode surface, which is similar to the observation at the end of the deposition stage (Figure 2i). Since the sharp trenches are still filled with deposited Zn layers, both the LEEs and the Zn stripping rates are uniform. As the stripping continues, the deposited Zn layer in the trench regions is removed, and the trench regions (circled by the black dashed line in Figure 3a and f) showed a much faster stripping rate than that of the protruding region (circled by the red dashed line in Figure 3a and f).

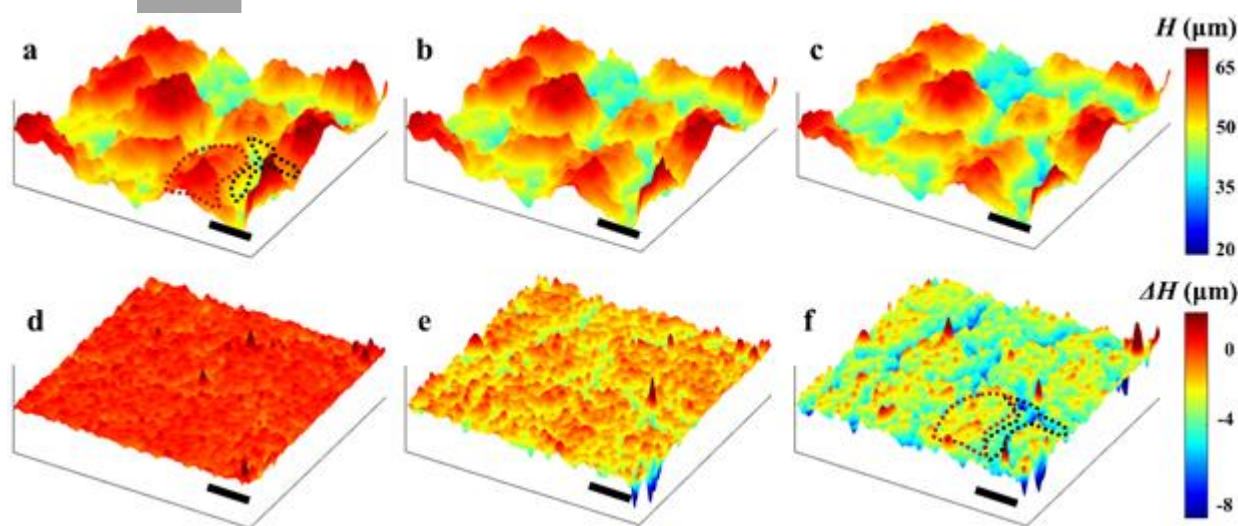


Figure. 3 Zn stripping dynamics. (a-c) The electrode tomography evolution after 0s, 770s and 1300s of stripping. (d-f) The thickness reduction for 210s, 770s and 1300s stripping. The scale bar is 30 μm .

2.4. Study LEE Effects on Electrode Reaction Using a Digital Twin.

Most of the LEE parameters cannot be directly measured, such as ion concentrations, current density, electric potential distributions, and overpotentials. To further understand the LEE effects on the metal deposition, we established a digital twin model that is a virtual replica of the real 3D Zn-Mn electrode. Utilizing the captured morphologies of the electrode surface at different stages of the reactions, we have developed a multiphysics finite element method (FEM) model to calculate the LEE parameters that cannot be measured directly from experiments. To build the digital twin, the 3D morphologies of the electrode at different time points were imported into the electroplating module in COMSOL Multiphysics as the cathode electrode (for Zn deposition), and a planar Zn electrode was used as the anode electrode. A constant current (80 mA cm^{-2}) was applied through the electrodes and the Zn ion concentration, electrolyte potential distribution, electrode surface overpotential, current density, and Zn deposition rate were simulated (Figure S6, Supporting Information).

It is very difficult to directly measure the LEE parameters experimentally, especially on a featured 3D electrode surface during the plating/stripping process. However, we have compared the deposition rate that is directly measured using the 3D microscope to the deposition rate that calculated by the digital twin to validate the accuracy of digital twin. Figure 2j shows the deposition rate at trench region (red curve to the left) and protruding region (black curve to the left) obtained and calculated from 3D microscope data. Figure 2k shows the deposition rate at trench region (red curve to the left) and protruding region (black curve to the left) calculated from the digital twin. The good agreement between the experimental results and digital twins indicates the viability of digital twin to explore the LEE parameters.

During the reactions, the geometry of 3D electrode will change significantly due to Zn deposition, which will lead to a totally different LEE and will influence the Zn deposition dynamics. Therefore, we compared the LEE at early ($t = 100$ s) and late ($t = 1300$ s) stages of deposition (Figure 4 and Figure S6, Supporting Information). At early stage of deposition, the electrode surface area per volume in the trench region is much higher than the protruding region. Therefore, the metal ions will be consumed at a much faster rate in the trenches than around the protruding regions and result in a lower ion concentration (Figure 4a, and the cross section inset). The concentration of Zn^{2+} can go as low as 1.6 M in the trench regions vs. 1.72 M around the protruding regions (Figure 4a). Low ion concentrations in trench regions will introduce a higher concentration gradient and lead to more efficient ion transport. As a result, the current densities in the trenches, especially at the bottom of the trenches, are significantly higher (~ 82 mA/cm² in Figure 4c) than those around the protruding regions (~ 72 mA/cm² in Figure 4b). In addition, the current densities in different trenches (Figure 4c) also vary due to their different geometry characteristics. Eventually, these current density variations will lead to different Zn deposition rates (~ 30 nm/s in the trench regions vs. ~ 15 nm/s on the protruding regions, Figure 4e). At the late stage of Zn deposition, the deep trench regions have been filled up due to their faster deposition rates (the inset in Figure 4b). The smoothed trenches will lead to a decreased ion consumption speed compared with that at the early stage of the deposition and a decreased concentration gradient in the trench regions (Figure 4b). The current density and the deposition rate in the trench regions will significantly decrease (Figure 4d and f) and the entire electrode surface shows a uniform Zn deposition rate (Figure 4f).

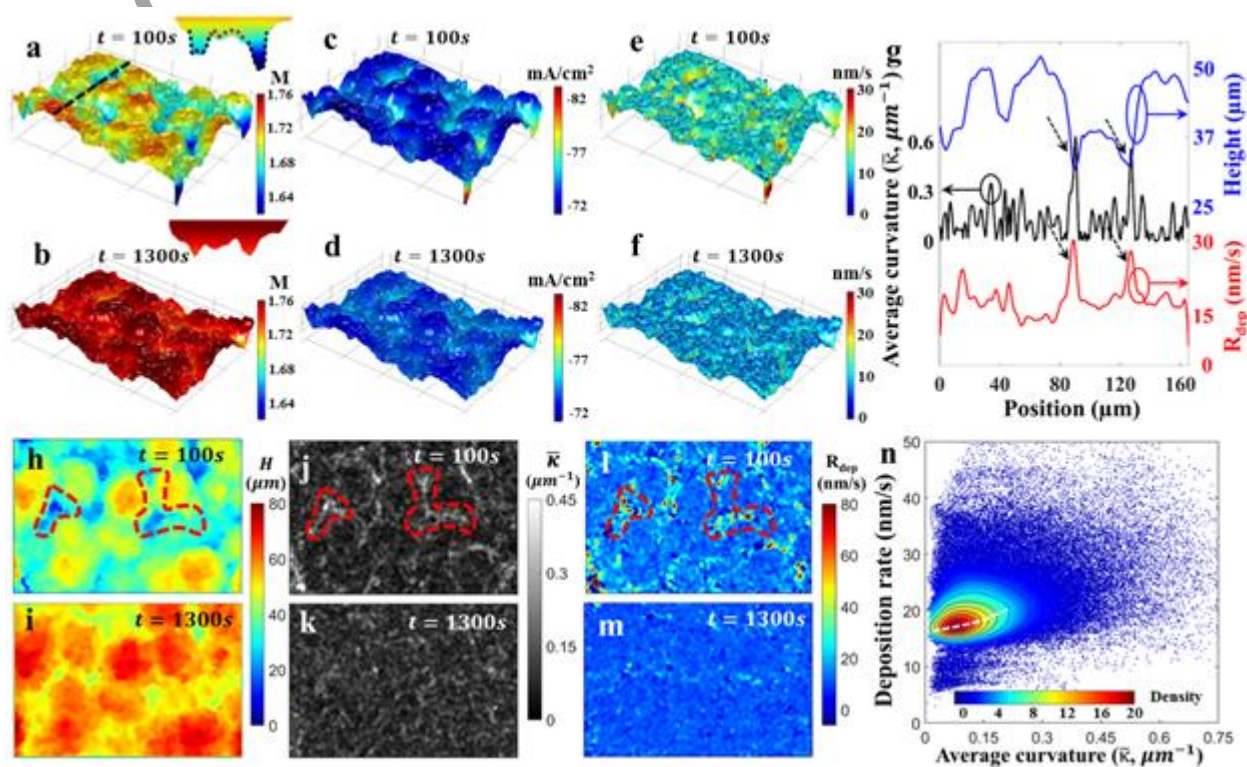


Figure. 4 Understand the LEEs effects on Zn depositions using digital twin. (a-b) Electrolyte concentration distribution at $t = 100$ s (a) and $t = 1300$ s (b). (c-d) Current density at $t = 100$ s (c) and $t = 1300$ s (d). (e-f) Deposition rate maps at $t = 100$ s (e) and $t = 1300$ s (f). All the LEE parameters are simulated using a digital twin, and the 3D geometries were obtained with the in-situ 3D microscopy and imported into the COMSOL Multiphysics model. (g) Mean curvature ($\bar{\kappa}_M$) (black curve, left axis), morphology/height (blue curve, right axis), and deposition rate (R_{dep}) (red curve, right axis) cross section profile along the black dashed line in Figure 4a. (h-i) 2D geometry (H) of Zn-Mn electrode at $t = 100$ s (h) and $t = 1300$ s (i). (j-k) Mean curvature ($\bar{\kappa}_M$) maps at $t = 100$ s

(j) and $t = 1300$ s (k). (l-m) Deposition rate (R_{dep}) at $t = 100$ s (l) and $t = 1300$ s (m). (n) The data density map to show the correlation between the Mean curvature and deposition rate. The data density map was plotted using the mean curvature and deposition rate calculated at each pixel in the region of observation. The scale bar is 30 μm .

2.5. The Geometry Effect on LEE and the Zn Depositions.

The geometry of 3D electrodes is the key that determines the LEE and affects Zn deposition dynamics. Therefore, it is important to find the relations between LEEs and the intrinsic geometry characteristics of 3D electrodes. We plotted the morphology profile of the electrode (blue line in Figure 4g), the mean curvature of the morphology profile (black curve in Figure 4g, see details about the calculation of mean curvature in the Methods section), and the deposition rate profile (red line in Figure 4g) along a cross section that cut through trenches and protruding regions (black dashed line in Figure 4a). We can see that there are two deep trench regions in the morphology profile pointed by black arrows in Figure 4g. The calculated curvature shows that they both have much bigger curvatures, more importantly, they both have a much bigger deposition rate which was measured from the experiment using the 3D microscopy (red curve in Figure 4g). This indicates that there might be a strong correlation between the curvature of the 3D morphology and the Zn deposition rate.

To further illustrate the relation between the curvature and the deposition rate, we have also plotted the 2D maps of electrode morphology (Figure 4h-i), calculated the mean curvature maps (Figure 4j-k), and the deposition rate maps (Figure 4l-m, measured from the experiment using the 3D microscopy) at early and late stages of the deposition. At the early stage of deposition, the trench regions are much deeper (red dashed circles in Figure 4h) and have bigger curvatures (red dashed circles in Figure 4j). Correspondingly, the deposition rates in the trench regions are much higher as well. On the other hand, the trenches were mostly filled up after a long time of deposition (Figure 4i). Therefore, the curvatures are much smaller and more uniform across the entire electrode, which will result in a smaller and uniform deposition rate across the surface at the late stage of the deposition. Our 3D microscopy has imaged the deposition rate maps at these two time points ($t = 100$ s and $t = 1300$ s), and we do find that the trench regions at $t = 100$ s are much higher than other regions (red dashed circles in Figure 4l, ~ 60 -80 nm/s in trench regions vs. ~ 25 nm/s in protruding regions). In addition, the Zn deposition rate is much smaller and more uniform at $t = 1300$ s (~ 15 nm/s across electrode surface). The deposition rate and the corresponded mean curvature at each location of 3D substrate is plotted in a data density map in Figure 4n. We can see the clear dependence between the curvature and the deposition rate. The average deposition rate is around 20 nm/s, and bigger curvature will lead to a bigger deposition rate (the white dashed line in Figure 4n). This evidence clearly shows the strong dependence of the LEE and the localized Zn deposition rate on the curvature of the 3D electrode surface and provides us a new method to control the deposition kinetics.

Metal deposition starts with nuclei formation and growth. LEEs will influence the nucleation location and density. We have used the *in-situ* 3D microscope to study the Zn nucleation distribution and density in the reaction process. Our 3D optical microscope is not able to detect small nuclei, which are normally defined as particles with a diameter from 1 to 5 nm.^[49] However, when the nuclei grow into larger particles with diameters more than 50 nm, the particles will scatter a significant amount of light away from the electrode surface and generate bright spots on our images. During the reaction, we recorded the image stacks at different time points with our 3D microscope. To obtain the Zn particle location and size distributions, we subtracted the image stack imaged at $t + \Delta t$ s with the image stack obtained at t s (Figure 5a, left and middle), and the differential image stacks showed many bright spots (Figure 5a right). Each bright spot is generated from the scattering of the Zn nanoparticle. Note that the subtraction was performed on the corresponded images that have the same height. The size information is obtained from a calibration experiment performed on a planar electrode surface (Figure S7, Supporting Information). The corresponded particle scattering intensity obtained from the optical microscope and the nanoparticle sizes obtained from the SEM image are plotted together, and the relation between size and scattering intensity is used to calibrate the particle size.

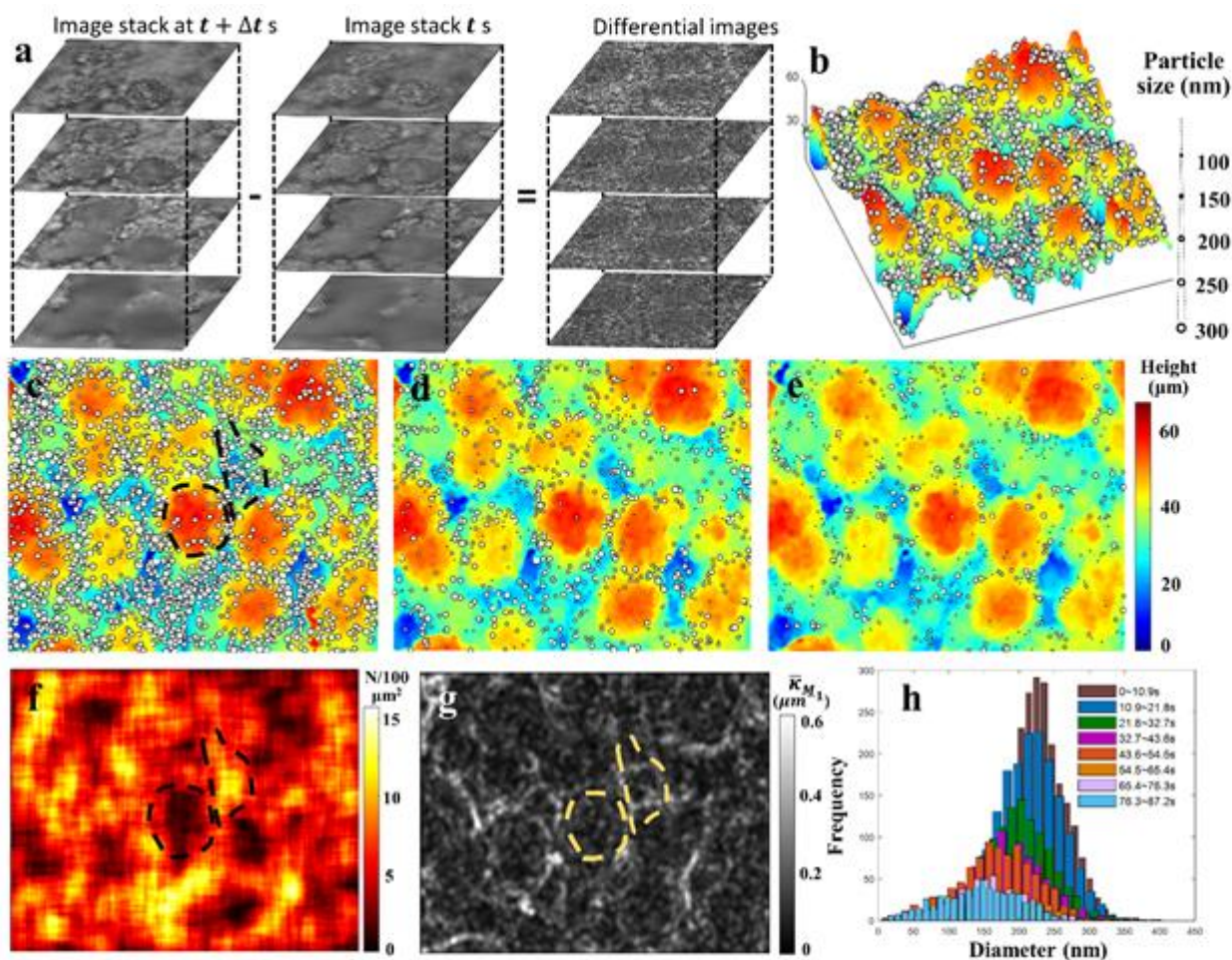


Figure. 5 Nucleation and growth dynamics. (a) Algorithm for Zn particle detection. (b) Zn nanoparticle size and location distributions on a 3D morphology map at 10 s. (c-e) Zn nanoparticle size and location distributions on a 2D map at 10 s, 50 s, and 80 s. (f) Zn nanoparticle density heat map at 10 s. (g) Curvature map of the electrode surface. (h) Particle size histogram at different times of reactions. The scale bar is 30 μm .

By using the Zn nanoparticle 3D location and size obtained from the image analysis, we can identify and plot the nanoparticle size and distribution on our 3D electrode morphology map. Figure 5c shows a Zn nanoparticle distribution map at $t = 10$ s, where the particle size is illustrated by the diameters of the circles. The trench regions show a much higher particle density comparing with the protruding region, and this is due to the geometry induced LEEs effect. Figure 5c-e (Figure S9, Supporting Information) show the particle size and location distributions at different stages of the reaction. At the early stage of the Zn deposition, the particle density is much higher. As the deposition continues, the growth rate decreases and the particle density also decreases. Figure 5h shows the histogram of the particle size distributions at different reaction times. The data also showed that as the reaction continues, the particle counts and the average sizes decrease. To better illustrate the particle distributions, we created the particle density heat maps (Figure 5f and Figure S8, Supporting Information). These maps clearly show that the trench regions (for example, the center black dashed circled in Figure 5c and f) have much higher particle density than the protruding regions (for example, the region circled by the black dashed lines in Figure 5c and f). We also plotted the 2D curvature map (Figure 5g) which is calculated from the 3D geometry of the electrode surface. The strong correlation between the particle density map (Figure 5f) and curvature map (Figure 5g) further demonstrates that the geometry will determine the LEEs and influence the reaction kinetics.

3. Conclusion

In conclusion, we studied the localized electrochemical environment's effect on electrode reaction dynamics. We found that the 3D geometry of the electrode will determine the localized electrochemical environments and the electrode reactions. We demonstrated that the reaction kinetics could be controlled by manipulating the LEEs using 3D geometry and the Zn dendrite could be minimized. An *in-situ* 3D microscope is developed to image the dynamics of Zn plating and stripping processes. 3D Zn-Mn alloy anodes were used as a model system which provides a 3D morphology that will greatly affect the LEEs. The Zn growth rate maps created by the 3D microscope showed that the reaction kinetics is highly correlated to the electrode geometry and the LEEs determined by the 3D morphology of Zn-Mn electrodes. We have employed a digital twin technique that allows us to create a virtual replica of the real Zn-Mn electrode and accurately simulate the LEEs, including localized ion concentrations and electric potential distributions. The results show that the localized ion concentration and geometry together determined the reaction kinetics and the dendrite formations. Zn nucleation density and distributions were extracted from the 3D microscope as well.

4. Experimental Section

In-situ optical 3D microscopy setup: The *in-situ* optical 3D microscope is built on an upright Olympus BX50 microscope. Since most Zn batteries operate in the high salt concentration aqueous electrolyte, such as 2 M ZnSO₄, the refractive index mismatch between the electrolyte and the air cause aberrations that blur the image. To minimize this effect, a 20X water immersion objective was used. The movement of the sample stage is controlled by a home-built motorized scanning stage. A motorized actuator (Thorlabs ZST225B) is programmed by the computer to control the vertical scanning speed. During the scanning, the objective lens is immersed in the electrolyte and the height of the lens is fixed. Instead, we control and scan the sample stage during the imaging process to change the objective-sample distance. A FLIR camera (Blackfly S USB3) was used to capture the 2D images at different heights. The camera frame rate and stage scanning speed is carefully selected to obtain enough cross-section images to rebuild 3D morphology. The optimized actuator scan speed is 16 μm/s and the camera framerate is 80 fps. The vertical interval between two images is tested and optimized to be around 200 nm for best height detection accuracy. In addition, to minimize the mechanical drift of the stage we have decreased the stage weight and developed a drift correction algorithm. This will allow us to correct the additional drift (Figure S3, Supporting Information). The 3D morphology were extracted from the image stack using variance and wavelet transfer methods.^[46, 47] These methods identify the focused point for each pixel and provide a height map for the entire 3D electrode surface. The axial resolution is determined by the depth of focus, which is in turn determined by the objective numerical aperture (NA). To obtain high-resolution 3D images in all three dimensions, a high NA water immersion objective is used. To balance the depth of focus, and x/y resolution, we used NA = 0.5 objective in this study.

Minimize the out of focus object's impact: The floating debris that are generated from the deposition and stripping process could float through the optical imaging path. However, these debris are mostly out of focus and their impacts to the sample imaging and focal plane detection is not significant. In addition, our multi-platform 3D reconstruction method has capabilities to remove smaller out of focus floating objects. We have also developed and implemented a small stirring/mixing system that will slowly circulate the electrolyte inside the reaction reservoir. The floating debris will be flush out quickly and their effects to the imaging process are minimized. If the floating debris significantly affect the 3D reconstruction, we could identify those frames and remove it automatically.

Electrolyte effects: Our 3D microscope is not sensitive to different types of aqueous electrolytes. To verify this, we did the 3D electrode scanning in the DI water, which has a biggest refractive index difference with the 2M ZnSO₄ electrolyte. As shown in the Figure S13 a-b, the trench regions and protruding regions in the optical image (Figure S13a, Supporting Information) are in good agreement with the reconstruction result (Fig. S13b, Supporting Information), and show similar structural features comparing with Figure 1 and Figure 2 in the manuscript. In addition, the optical images are

also recorded in two other electrolytes: (1) 2 M ZnSO₄ with 0.1 M MnSO₄ (Figure S13c, Supporting Information); (2) 2 M ZnSO₄ with 0.1 M MnSO₄ in seawater (Figure S13d, Supporting Information). We can easily observe that the optical images share similar imaging quality even in different electrolytes, which will all lead to high quality 3D reconstruction results. Therefore, we believe that different electrolytes will not influence our 3D microscope and the same reconstruction protocol can be used.

3D Zn-Mn electrode fabrication: The 3D structured Zn-Mn electrode is prepared by an alloy electrodeposition approach. All 3D structured Zn-Mn alloys were electrodeposited on Zn substrates (99.95% metals basis, 0.25 mm thick, Alfa AesarTM). In all, 100 mL deionized (DI) water was pre-heated at 80 °C as the solvent to dissolve 0.2 M zinc sulfate heptahydrate (ZnSO₄·7H₂O, Fisher Chemical), 0.2M sodium citrate dihydrate (Granular/Certified), and 0.6 M ethylenediaminetetraacetic acid disodium salt dihydrate (Crystalline/Certified ACS, Fisher Chemical) under continuous stirring for 30 min (noted as Solution A). Then, 0.6 M manganese (II) sulfate monohydrate (MnSO₄·H₂O, 99+%, extra pure, ACROS OrganicsTM) was added to Solution A and stirred for another 30 min until a transparent solution was obtained (noted as

Solution B). In a two-electrode electrochemical cell, with the Zn substrate as the working electrode and the platinum mesh as the counter electrode, the current density of 0.3 A cm⁻² is performed to co-deposit both Zn²⁺ and Mn²⁺ ions for 40 min in solution B. During the electrodeposition, continuous H₂ bubbles will generate at the solid-liquid interface because of water dissociation under extremely high current density condition to work as gaseous templates, leading to the formation of 3D structures.

Electrochemical test: A two-electrode system is used in this study, with 3D Zn-Mn alloy substrate as working electrode (cathode), pristine Zn foil as counter and reference electrodes (anode) and 2M ZnSO₄ in DI water as the electrolyte. A special electrochemical cell with a size of 1 cm× 1 cm× 2 mm is designed using polydimethylsiloxane (PDMS, prepared by the mixing of base elastomer and curing agent with a ratio of 10:1 and then cross-linking for 1 h at 90 °C) to hold about 1ml electrolyte and both cathode and anode were immersed in the electrolyte. Both the plating and stripping processes are performed with CHI660E (CH Instrument Ins.) with a constant current density of 80mA cm⁻².

Geometry characteristic calculation: Curvature usually indicates the amount by which a surface deviates from being a plane. There are infinite orthogonal curvatures for a certain point on the curved surface, among which, there will be a curve that owns the maximum value of curvature, representing by k_{max} , and the curvature perpendicular to the maximum curvature surface is the minimum curvature, k_{min} . These two curvatures are defined as main curvatures. The Gaussian curvature is equal to the product of the principal curvatures, that is

$$k_G = k_{max} * k_{Gmin} \quad (1)$$

It has the dimension of length⁻², and the mean curvature is defined as the half the sum of the principle curvatures,

$$k_M = \frac{k_{max} + k_{Gmin}}{2} \quad (2)$$

Thus, the mean curvature has a dimension of length⁻¹. Since the Gaussian curvature does not depend on the embedding of the surface and mainly indicate the intrinsic property of the surface which is not the focus in this case. Therefore, the mean curvature is adopted in our analysis because it measures the degree of bending of a surface in the space which will have significant influence on localized surface features and impact the LEEs.

Digital twin simulation: A digital twin is constructed with COMSOL to carefully study the impact of localized electrochemical environments on electrochemical process. The initial 3D substrate without going any reactions is firstly reconstructed by our multi-platform 3D reconstruction method and then imported into the COMSOL as the cathode. So that the working electrode for both practical experiment and digital twin can keep the maximum degree of consistency and will share the same geometry features. The whole cell set up is modeled by a block, with the imported substrate at the bottom as cathode, and the upper horizontal planar as the anode. The vertical walls correspond to the

cell reservoir boundary and are assumed to be insulating (Figure S6, Supporting Information). Similarly, on the cathode, the current density of 800 A m^{-2} (80 mA cm^{-2}) is applied as the boundary condition to match the actual experimental condition. During the electroplating process, the electrode morphology will keep changing due to continuously plating occurs on the electrode, which will influence the LEEs simultaneously. Therefore, another digital twin with the 3D morphology obtained at the end of the practical deposition reaction is constructed to calculate the corresponding LEEs (Figure S6d, Supporting Information). In addition to electrolyte concentration and current density distribution, the electrolyte potentials and electrode surface overpotentials of two digital twins are also plotted. The electrolyte potentials (Figure S6b-e, Supporting Information) indicate a positive correlation with the distance between the working electrode and the counter electrode, showing that the electrolyte potential at protrude structures is a little bit higher than that at the deep trench areas. This is reasonable because the electrochemical potential of the species in the solution is defined as the sum of chemical potential and Galvani potential, thus the farther away from the counter electrode, more energy needed to overcome the electrostatic attraction, and smaller the electrochemical potential. Overpotential is another important factor that could determine the reaction activities. According to the Nernst equation, the overpotential of the reaction is closely related to the electrolyte concentration. We have plotted the overpotential distributions in Figure S6c-f, Supporting Information), and only minimal variations at different locations can be observed. This may because the electrolyte concentration in our experiment is very high (2 M ZnSO_4), so the electrolyte concentration decrease in trench region is in-significant to generate big overpotential variations. Therefore, the localized overpotential difference is not the key factor that impact the reaction kinetics in our case.

Supporting Information

Supporting Information is available from the Wiley Online Library or from the author.

Acknowledgements

This work was supported by the start-up at the University of Houston, the University of Houston's High Priority Area Research Equipment Grant, University of Houston Center for Carbon Management in Energy program, support from Beyond Bits Technology, Inc., and Department of Energy (DOE DE-FE-0032092) (X.S.). Y.Y. acknowledges financial support from the National Science Foundation under Grant No. CMMI-1851674 and CBET-1949840. D.M. acknowledges financial support from the National Science Foundation under Grant NSF CAREER 1943455.

Conflict of Interest

The authors declare that they have no conflict of interest.

Data Availability Statement

The data that support the findings of this study are available from the corresponding authors upon reasonable request.

Keywords

localized electrochemical environment; *in-situ* 3D microscope; digital twin; 3D morphology dynamics; control reaction kinetics; dendrite-free.

References

- [1] J. B. Goodenough, K. S. Park, *Journal of the American Chemical Society* 2013, 135, 1167.
- [2] B. Dunn, H. Kamath, J. M. Tarascon, *Science* 2011, 334, 928.
- [3] L. Grande, E. Paillard, J. Hassoun, J. B. Park, Y. J. Lee, Y. K. Sun, S. Passerini, B. Scrosati, *Advanced Materials* 2015, 27, 784.
- [4] Y. Y. Lu, M. Tikekar, R. Mohanty, K. Hendrickson, L. Ma, L. A. Archer, *Adv. Energy Mater.* 2015, 5, 7.
- [5] A. S. Arico, P. Bruce, B. Scrosati, J. M. Tarascon, W. Van Schalkwijk, *Nat. Mater.* 2005, 4, 366.
- [6] Y. M. Sun, N. A. Liu, Y. Cui, *Nat. Energy* 2016, 1, 12.
- [7] X. B. Cheng, Q. Zhang, *J. Mater. Chem. A* 2015, 3, 7207.
- [8] J. M. Tarascon, M. Armand, *Nature* 2001, 414, 359.
- [9] Y. P. Guo, H. Q. Li, T. Y. Zhai, *Advanced Materials* 2017, 29, 25.
- [10] H.-F. Wang, Q. Xu, *Matter* 2019, 1, 565.
- [11] H. Liu, X.-B. Cheng, Z. Jin, R. Zhang, G. Wang, L.-Q. Chen, Q.-B. Liu, J.-Q. Huang, Q. Zhang, *EnergyChem* 2019, 1, 100003.
- [12] Q. Liu, Z. Pan, E. Wang, L. An, G. Sun, *Energy Storage Materials* 2020, 27, 478.
- [13] N. W. Li, Y. X. Yin, C. P. Yang, Y. G. Guo, *Advanced materials* 2016, 28, 1853.
- [14] Y. Liu, D. Lin, P. Y. Yuen, K. Liu, J. Xie, R. H. Dauskardt, Y. Cui, *Advanced Materials* 2017, 29, 1605531.
- [15] N. W. Li, Y. Shi, Y. X. Yin, X. X. Zeng, J. Y. Li, C. J. Li, L. J. Wan, R. Wen, Y. G. Guo, *Angewandte Chemie International Edition* 2018, 57, 1505.
- [16] S. Chen, J. Zheng, D. Mei, K. S. Han, M. H. Engelhard, W. Zhao, W. Xu, J. Liu, J. G. Zhang, *Advanced materials* 2018, 30, 1706102.
- [17] X. Ren, S. Chen, H. Lee, D. Mei, M. H. Engelhard, S. D. Burton, W. Zhao, J. Zheng, Q. Li, M. S. Ding, *Chem* 2018, 4, 1877.
- [18] H. Zhao, D. Lei, Y. B. He, Y. Yuan, Q. Yun, B. Ni, W. Lv, B. Li, Q. H. Yang, F. Kang, *Adv. Energy Mater.* 2018, 8, 1800266.
- [19] N. Liu, Z. Lu, J. Zhao, M. T. McDowell, H.-W. Lee, W. Zhao, Y. Cui, *Nature nanotechnology* 2014, 9, 187.
- [20] X. B. Cheng, T. Z. Hou, R. Zhang, H. J. Peng, C. Z. Zhao, J. Q. Huang, Q. Zhang, *Advanced materials* 2016, 28, 2888.
- [21] M. Xu, D. Ivey, Z. Xie, W. Qu, *J. Power Sources* 2015, 283, 358.
- [22] K. Yan, Z. D. Lu, H. W. Lee, F. Xiong, P. C. Hsu, Y. Z. Li, J. Zhao, S. Chu, Y. Cui, *Nat. Energy* 2016, 1, 8.
- [23] J. Liu, Z. Bao, Y. Cui, E. J. Dufek, J. B. Goodenough, P. Khalifah, Q. Li, B. Y. Liaw, P. Liu, A. Manthiram, *Nat. Energy* 2019, 4, 180.
- [24] H. Sun, J. Zhu, D. Baumann, L. Peng, Y. Xu, I. Shakir, Y. Huang, X. Duan, *Nat. Rev. Mater.* 2019, 4, 45.
- [25] H. J. Peng, W. T. Xu, L. Zhu, D. W. Wang, J. Q. Huang, X. B. Cheng, Z. Yuan, F. Wei, Q. Zhang, *Adv. Funct. Mater.* 2016, 26, 6351.
- [26] W. Liu, Z. Chen, G. Zhou, Y. Sun, H. R. Lee, C. Liu, H. Yao, Z. Bao, Y. Cui, *Advanced materials* 2016, 28, 3578.
- [27] Y. Xu, Z. Lin, X. Zhong, X. Huang, N. O. Weiss, Y. Huang, X. Duan, *Nat. Commun.* 2014, 5, 1.
- [28] M. Zier, F. Scheiba, S. Oswald, J. Thomas, D. Goers, T. Scherer, M. Klose, H. Ehrenberg, J. Eckert, *J. Power Sources* 2014, 266, 198.

- [29] J. T. Lee, N. Nitta, J. Benson, A. Magasinski, T. F. Fuller, G. Yushin, *Carbon* 2013, 52, 388.
- [30] B. Xiang, L. Wang, G. Liu, A. M. Minor, *J. Electrochem. Soc.* 2013, 160, A415.
- [31] J. Y. Huang, L. Zhong, C. M. Wang, J. P. Sullivan, W. Xu, L. Q. Zhang, S. X. Mao, N. S. Hudak, X. H. Liu, A. Subramanian, H. Y. Fan, L. A. Qi, A. Kushima, J. Li, *Science* 2010, 330, 1515.
- [32] X. H. Liu, J. W. Wang, S. Huang, F. F. Fan, X. Huang, Y. Liu, S. Krylyuk, J. Yoo, S. A. Dayeh, A. V. Davydov, S. X. Mao, S. T. Picraux, S. L. Zhang, J. Li, T. Zhu, J. Y. Huang, *Nature Nanotechnology* 2012, 7, 749.
- [33] F. Wang, H. C. Yu, M. H. Chen, L. J. Wu, N. Pereira, K. Thornton, A. Van der Ven, Y. M. Zhu, G. G. Amatucci, J. Graetz, *Nat. Commun.* 2012, 3, 8.
- [34] M. Gu, L. R. Parent, B. L. Mehdi, R. R. Unocic, M. T. McDowell, R. L. Sacci, W. Xu, J. G. Connell, P. H. Xu, P. Abellan, X. L. Chen, Y. H. Zhang, D. E. Perea, J. E. Evans, L. J. Lauhon, J. G. Zhang, J. Liu, N. D. Browning, Y. Cui, I. Arslan, C. M. Wang, *Nano Lett.* 2013, 13, 6106.
- [35] Z. Y. Zeng, W. I. Liang, H. G. Liao, H. L. L. Xin, Y. H. Chu, H. M. Zheng, *Nano Lett.* 2014, 14, 1745.
- [36] B. L. Mehdi, J. Qian, E. Nasybulin, C. Park, D. A. Welch, R. Faller, H. Mehta, W. A. Henderson, W. Xu, C. M. Wang, J. E. Evans, J. Liu, J. G. Zhang, K. T. Mueller, N. D. Browning, *Nano Lett.* 2015, 15, 2168.
- [37] R. L. Sacci, J. M. Black, N. Balke, N. J. Dudney, K. L. More, R. R. Unocic, *Nano Lett.* 2015, 15, 2011.
- [38] Y. Z. Li, Y. B. Li, A. L. Pei, K. Yan, Y. M. Sun, C. L. Wu, L. M. Joubert, R. Chin, A. L. Koh, Y. Yu, J. Perrino, B. Butz, S. Chu, Y. Cui, *Science* 2017, 358, 506.
- [39] X. F. Wang, M. H. Zhang, J. Alvarado, S. Wang, M. Sina, B. Y. Lu, J. Bouwer, W. Xu, J. Xiao, J. G. Zhang, J. Liu, Y. S. Meng, *Nano Lett.* 2017, 17, 7606.
- [40] J. W. Gallaway, A. M. Gaikwad, B. Hertzberg, C. K. Erdonmez, Y.-c. K. Chen-Wiegart, L. A. Sviridov, K. Evans-Lutterodt, J. Wang, S. Banerjee, D. A. Steingart, *J. Electrochem. Soc.* 2013, 161, A275.
- [41] R. Bhattacharyya, B. Key, H. Chen, A. S. Best, A. F. Hollenkamp, C. P. Grey, *Nat. Mater.* 2010, 9, 504.
- [42] K. Nishikawa, T. Mori, T. Nishida, Y. Fukunaka, M. Rosso, T. Homma, *J. Electrochem. Soc.* 2010, 157, A1212.
- [43] E. R. White, S. B. Singer, V. Augustyn, W. A. Hubbard, M. Mecklenburg, B. Dunn, B. C. Regan, *ACS Nano* 2012, 6, 6308.
- [44] Q. Ma, X. X. Zeng, J. Yue, Y. X. Yin, T. T. Zuo, J. Y. Liang, Q. Deng, X. W. Wu, Y. G. Guo, *Adv. Energy Mater.* 2019, 9, 1803854.
- [45] V. Yufit, F. Tariq, D. S. Eastwood, M. Biton, B. Wu, P. D. Lee, N. P. Brandon, *Joule* 2019, 3, 485.
- [46] B. Forster, D. Van De Ville, J. Berent, D. Sage, M. Unser, *Microscopy research and technique* 2004, 65, 33.
- [47] L. R. de Oliveira Hein, J. A. De Oliveira, K. A. De Campos, P. C. R. De Oliveira Caltabiano, *Microscopy research and technique* 2012, 75, 1593.
- [48] H. Tian, Z. Li, G. Feng, Z. Yang, D. Fox, M. Wang, H. Zhou, L. Zhai, A. Kushima, Y. Du, *Nat. Commun.* 2021, 12, 1.
- [49] A. Pei, G. Y. Zheng, F. F. Shi, Y. Z. Li, Y. Cui, *Nano Lett.* 2017, 17, 1132.
- [50] Y. Sun, S. Duthaler, B. J. Nelson, *Microscopy research and technique* 2004, 65, 139.

The effect of the localized electrochemical environment (LEE) on the metal batteries' reaction kinetics is studied by using novel *in-situ* 3D microscopy and a digital twin. The LEEs, such as local current density, ion concentration and potentials, are extracted. We demonstrated and proved that the LEE will determine the localized reaction kinetics and the dendrite formation in 3D electrodes.

Author Manuscript